

A CRITICAL ASSESSMENT OF NONLINEAR FORCE-FREE FIELD MODELING OF THE SOLAR CORONA FOR ACTIVE REGION 10953

MARC L. DEROSA¹, CAROLUS J. SCHRIJVER¹, GRAHAM BARNES², K. D. LEKA², BRUCE W. LITES³, MARKUS J. ASCHWANDEN¹, TAHAR AMARI^{4,5}, AURÉLIEN CANOU⁴, JAMES M. McTIERNAN⁶, STÉPHANE RÉGNIER⁷, JULIA K. THALMANN⁸, GHERARDO VALORI⁹, MICHAEL S. WHEATLAND¹⁰, THOMAS WIEGELMANN⁸, MARK C. M. CHEUNG¹, PAUL A. CONLON¹¹, MARCEL FUHRMANN¹², BERND INHESTER⁸, AND TILAYE TADESSE^{8,13}

¹ Lockheed Martin Solar and Astrophysics Laboratory, 3251 Hanover St. B/252, Palo Alto, CA 94304, USA

² North West Research Associates, Colorado Research Associates Division, 3380 Mitchell Ln., Boulder, CO 80301, USA

³ High Altitude Observatory, National Center for Atmospheric Research¹⁴, P.O. Box 3000, Boulder, CO 80307, USA

⁴ CNRS, Centre de Physique Théorique de l'École Polytechnique, 91128 Palaiseau Cedex, France

⁵ LESIA, Observatoire de Paris, 5 Place Jules Janssen, 92190 Meudon Cedex, France

⁶ Space Sciences Laboratory, University of California at Berkeley, 7 Gauss Way, Berkeley, CA 94720, USA

⁷ Mathematics Institute, University of St Andrews, St Andrews, Fife KY16 9SS, UK

⁸ Max-Planck-Institut für Sonnensystemforschung, Max-Planck-Strasse 2, 37191 Katlenburg-Lindau, Germany

⁹ Astrophysikalisches Institut Potsdam, An der Sternwarte 16, 14482 Potsdam, Germany

¹⁰ School of Physics, University of Sydney, Sydney, NSW 2006, Australia

¹¹ Astrophysics Research Group, School of Physics, Trinity College Dublin, Dublin 2, Republic of Ireland

¹² Institut für Physik, Universität Potsdam, Am Neuen Palais 10, 14469 Potsdam, Germany

¹³ Department of Physics, Addis Ababa University, P.O. Box 1176, Addis Ababa, Ethiopia

Received 2008 November 13; accepted 2009 February 18; published 2009 April 27

ABSTRACT

Nonlinear force-free field (NLFFF) models are thought to be viable tools for investigating the structure, dynamics, and evolution of the coronae of solar active regions. In a series of NLFFF modeling studies, we have found that NLFFF models are successful in application to analytic test cases, and relatively successful when applied to numerically constructed Sun-like test cases, but they are less successful in application to real solar data. Different NLFFF models have been found to have markedly different field line configurations and to provide widely varying estimates of the magnetic free energy in the coronal volume, when applied to solar data. NLFFF models require consistent, force-free vector magnetic boundary data. However, vector magnetogram observations sampling the photosphere, which is dynamic and contains significant Lorentz and buoyancy forces, do not satisfy this requirement, thus creating several major problems for force-free coronal modeling efforts. In this paper, we discuss NLFFF modeling of NOAA Active Region 10953 using *Hinode*/SOT-SP, *Hinode*/XRT, *STEREO*/SECCHI-EUVI, and *SOHO*/MDI observations, and in the process illustrate three such issues we judge to be critical to the success of NLFFF modeling: (1) vector magnetic field data covering larger areas are needed so that more electric currents associated with the full active regions of interest are measured, (2) the modeling algorithms need a way to accommodate the various uncertainties in the boundary data, and (3) a more realistic physical model is needed to approximate the photosphere-to-corona interface in order to better transform the forced photospheric magnetograms into adequate approximations of nearly force-free fields at the base of the corona. We make recommendations for future modeling efforts to overcome these as yet unsolved problems.

Key words: Sun: corona – Sun: magnetic fields

1. INTRODUCTION

The structure and evolution of the magnetic field (and the associated electric currents) that permeates the solar atmosphere play key roles in a variety of dynamical processes observed to occur on the Sun. Such processes range from the appearance of extreme ultraviolet (EUV) and X-ray bright points, to brightenings associated with nanoflare events, to the confinement and redistribution of coronal loop plasma, to reconnection events, to X-ray flares, to the onset and liftoff of the largest mass ejections. It is believed that many of these observed phenomena take on different morphologies depending on the configurations of the magnetic field, and thus knowledge of such field configurations is becoming an increasingly important factor in discriminating between different classes of events. The coronal topology is thought to be a critical factor in determining, for example, why

some active regions flare, why others do not, how filaments form, and many other topics of interest.

One model of the coronal magnetic field \mathbf{B} assumes that the corona is static and free of Lorentz forces, such that $\mathbf{J} \times \mathbf{B} = \mathbf{0}$, where $\mathbf{J} = c \nabla \times \mathbf{B} / 4\pi$ is the current density. This means that $\nabla \times \mathbf{B} = \alpha \mathbf{B}$, and thus any electric currents must be aligned with the magnetic field. Because $\nabla \cdot \mathbf{B} = 0$, it can be shown that $\mathbf{B} \cdot \nabla \alpha = 0$, demonstrating that α is invariant along field lines of \mathbf{B} . The scalar α is in general a function of space and identifies how much current flows along each field line. In cases where α varies spatially, the problem of solving for \mathbf{B} (and α) is nonlinear. Solving for such nonlinear force-free fields (NLFFFs) requires knowledge of \mathbf{B} over the complete bounding surface S enclosing the solution domain. To be compatible with a force-free field, it is necessary for these boundary data $\mathbf{B}|_S$ to satisfy a number of consistency criteria, which we outline in Section 2 and which are explained in detail by Molodenskii (1969) and Aly (1984, 1989).

¹⁴ The National Center for Atmospheric Research is sponsored by the National Science Foundation.

In analyzing solar active regions, localized maps of the photospheric vector field are typically used for the lower bounding surface $\mathbf{B}|_{z_0}$, and potential fields are used for the other surfaces. (For the Cartesian models discussed herein, we use the convention that the z axis is normal to the photosphere, which is located at height $z = z_0$.) The availability of vector field maps, produced by recent instrument suites such as the Synoptic Optical Long-term Investigations of the Sun (SOLIS) facility and the *Hinode* spacecraft, building on earlier work done in Hawaii with data from the Haleakalā Stokes Polarimeter (HSP) and by the Imaging Vector Magnetograph (IVM) as well as from the HAO/NSO Advanced Stokes Polarimeter (ASP) at Sacramento Peak in New Mexico, has spurred investigations that employ coronal field models based on such measurements. We anticipate that such research will intensify when regular, space-based vector field maps from the Helioseismic and Magnetic Imager (HMI) instrument on board the *Solar Dynamics Observatory* (SDO) become available.

One goal of NLFFF modeling is to provide useful estimates of physical quantities of interest (e.g., connectivities, free energies, and magnetic helicities) for ensembles of active regions, so that these active regions may be systematically analyzed and intercompared. The use of static, force-free models mitigates some of the computational difficulties associated with solving the more physically realistic, time-dependent problem, as running such dynamical models at the desired spatial and temporal resolutions for multiple active regions typically exceeds current computing capabilities.

There exist several previous studies of individual active regions where NLFFF models are shown to be compatible with various structures in the corona (e.g., Régnier et al. 2002; Régnier & Amari 2004; Wiegelmann et al. 2005; Régnier & Canfield 2006; Schrijver et al. 2008). Several of these studies provide evidence of good alignment between NLFFF model field lines and the locations of observed features such as coronal loop structures observed in EUV and X-ray images. Others show that the locations of sigmoids, twisted flux ropes, and/or field line dip locations coincide with analogous features in the NLFFF models. Such studies are certainly encouraging, but still it remains difficult to conclusively determine whether these models match a significant fraction of the coronal magnetic field located within the volume overlying an entire active region.

As part of a long-lasting (e.g., Sakurai 1981; McClymont et al. 1997) effort to develop methods that generate more robust NLFFF models, a working group (in which all of the authors of this paper are participating) has held regular workshops over the past several years. The previous results from this collaboration are presented by Schrijver et al. (2006), Metcalf et al. (2008), and Schrijver et al. (2008). Since the launch of *Hinode* in 2006, we have applied multiple NLFFF modeling codes to a few active regions for which *Hinode* vector magnetogram data are available and for which nonpotential features are evident (e.g., Schrijver et al. 2008). The resulting NLFFF models generally differ from each other in many aspects, such as the locations and magnitudes of currents, as well as measurements of magnetic energy in the solution domain. In this paper, we identify several problematic issues that plague the NLFFF-modeling endeavor, and use a recent *Hinode* case to illustrate these difficulties. We describe one representative data preparation scheme in Section 2, followed in Section 3 by a comparison of field lines in the resulting NLFFF models to two- and three-dimensional coronal loop paths, the latter determined by analyzing pairs

of stereoscopic images. In Section 4, we explain the primary issues that we believe to impact our ability to reconstruct the coronal field in a robust manner, and also identify and discuss the alternate data preparation scenarios we tried in addition to those presented in Section 2. Concluding remarks are presented in Section 5.

2. CONSTRUCTION OF NLFFF MODELS FOR AR 10953

Several NLFFF extrapolation algorithms (each implementing one of the three general classes of extrapolation methods) were applied to boundary conditions deduced from a scan of NOAA Active Region (AR) 10953, taken by the Spectro-Polarimeter (SP) instrument of the Solar Optical Telescope (SOT; Tsuneta et al. 2008) on board the *Hinode* spacecraft. The *Hinode*/SOT-SP scan of this active region started at UT 22:30 on 2007 April 30 and took about 30 min to complete. As the scan progressed, polarization spectra of two magnetically sensitive Fe I lines at 6301.5 Å and 6302.5 Å were obtained within the $0'.16 \times 164''$ slit, from which Stokes IQUV spectral images were generated. For this scan (in “fast-map” mode), the along-slit and slit-scan sampling was $0'.32$, and the total width of the scan was $160''$. AR 10953 produced a C8.5 flare about two days after this *Hinode*/SOT-SP scan, and a C4.2 flare about four and a half days after this scan, but otherwise the active region was flare-quiet above the C1.0 level. Images from the X-ray Telescope (XRT; Golub et al. 2007) on board *Hinode* around this time show a series of bright loops in the central region of AR 10953 (Figure 1(a)).

The NLFFF algorithms need vector magnetic data as boundary conditions, and determining these boundary maps comprises the first step in constructing NLFFF models. The conditions pertaining to the lower boundary are determined from a map of the photospheric vector magnetic field from the *Hinode*/SOT-SP instrument. The magnetic components parallel to and transverse to the line of sight, B_{LOS} and \mathbf{B}_t , are functions of the circular and linear polarization signals, respectively. Constructing $\mathbf{B}|_{z_0}$ requires assuming an atmospheric model (in this case Milne-Eddington) and determining which combinations of magnetic field strengths and filling factors produce the observed polarization signals (e.g., Skumanich & Lites 1987; Klimchuk et al. 1992; Borrero et al. 2007). B_{LOS} has uncertainties that are typically an order of magnitude less than \mathbf{B}_t .

The next step involves removing the ambiguities in the components of \mathbf{B}_t that arise due to the property that the same linear polarization signal can be produced by either of two magnetic field vectors differing by 180° of azimuth in the transverse plane. We choose to perform the disambiguation using the interactive Azimuthal Ambiguity Method (AZAM), which is one of several methods that have been devised and tested to resolve this ambiguity (see Metcalf et al. 2006, and references therein).

After disambiguation, the $\mathbf{B}|_{z_0}$ map for AR 10953 is used to produce potential field data with which the extrapolation codes will initialize the computational domain. Our approach is to specify the computational domain (having an enclosing surface S) that contains much of the coronal volume overlying the active region of interest, such that the lower boundary includes the area for which vector magnetogram data are available. The initialization field is calculated by embedding the *Hinode*/SOT-SP vector magnetogram data in a larger line-of-sight magnetogram observed by the Michelson Doppler

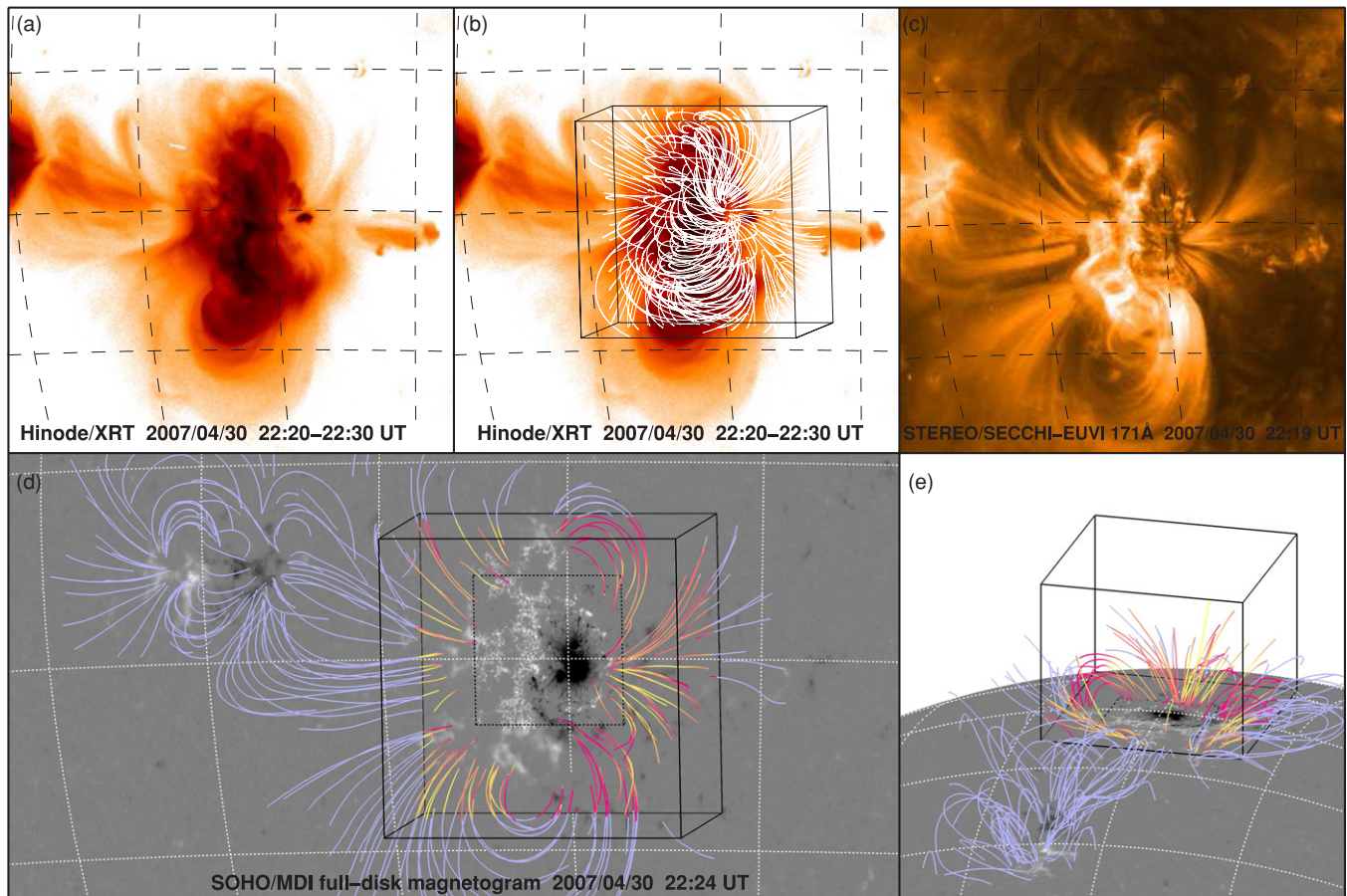


Figure 1. Series of co-aligned images of AR 10953 (with the same 10° gridlines drawn on all images for reference). (a) Time-averaged and logarithmically scaled *Hinode*/XRT soft X-ray image, and (b) with the best-fit Wh^- model field lines overlaid. (c) *STEREO-A*/SECCHI-EUVI 171 Å image. (d) Trajectories of loops, as viewed from the perspective of an observer located along the Sun–Earth line of sight and determined stereoscopically from contemporaneous pairs of images from the two *STEREO* spacecraft. (e) Same visualization as panel (d) but viewed from the side. The solid black cubes in panels (d) and (e) outline the full $320 \times 320 \times 256$ pixel NLFFF computational domain, and the interior dotted black square outlines the base of the smaller $160 \times 160 \times 160$ pixel volume (covering most of the *Hinode*/SOT-SP scan area) used for the field line maps of Figure 2 and for the metrics in Table 1. The *STEREO*-loop points are colored blue if outside the NLFFF computational domain, or are colored according to their misalignment angle ϕ made with the field lines from the Wh^- solution. Yellow is indicative of $\phi < 5^\circ$, red of $\phi > 45^\circ$, with a continuous progression from yellow through orange to red for $5^\circ < \phi < 45^\circ$. On the bottom face of the large cube is displayed the B_z map used during the NLFFF modeling, which includes higher resolution data from *Hinode*/SOT-SP embedded in *SOHO*/MDI full-disk magnetogram data. The magnetogram images saturate at $\pm 1500 \text{ Mx cm}^{-2}$.

Imager (MDI) instrument (Scherrer et al. 1995) on board the *Solar and Heliospheric Observatory* (*SOHO*) spacecraft (as shown in Figure 1(d)). Then, the potential field coefficients corresponding to this enlarged footprint are determined, from which the potential field in the $320 \times 320 \times 256$ pixel NLFFF computational domain is computed. In addition, the vector field boundary conditions for the side and top boundaries of the computational domain are taken from this same potential field extrapolation, primarily because we expect that the coronal magnetic field becomes largely potential away from the center of the active region, but also because it is useful to specify how unbalanced flux emanating from this active region connects to flux of the opposite polarity located elsewhere on the Sun.

The embedded lower boundary data are then sampled onto a uniform, helioplanar, 320×320 pixel grid having 580 km pixels, such that the footprint of the computational domain spans a 185.6 Mm square area. The region for which *Hinode* vector magnetogram data for AR 10953 were available comprise about a $100 \text{ Mm} \times 115 \text{ Mm}$ subarea of the full lower boundary footprint, outside of which the horizontal components of $\mathbf{B}|_{z_0}$ are set to zero. Thus, in this peripheral region outside the *Hinode*/SOT-SP field of view, the field on the lower boundary can

be considered either as purely vertical (for force-free methods which use all three components of the field as boundary conditions), or equivalently as having zero vertical current density (for methods which use the vertical component of the field together with the vertical component of the current density).

Next, to be consistent with a force-free field, it is necessary (but not sufficient) that the entire boundary field $\mathbf{B}|_S$ satisfy several criteria, as delineated by Molodenskii (1969) and Aly (1984, 1989), namely: (1) the volume-integrated Lorentz force must vanish, (2) the volume-integrated magnetic torque must vanish, and (3) the amount of negative-polarity flux through $\mathbf{B}|_S$ having a given value of α must equal the positive-polarity flux through $\mathbf{B}|_S$ with this same value of α . The first two criteria are relations involving various components of $\mathbf{B}|_S$, and are derived from volume integrals of the Lorentz force and its first moment. The third (“ α -correspondence”) relation operates over all values of α present on $\mathbf{B}|_S$.

There is, of course, no guarantee, however, that the values of $\mathbf{B}|_{z_0}$, coupled with the potential field of \mathbf{B} for the complement of the enclosing surface, together satisfy these consistency criteria. Our working group attempts to deal with this problem by preprocessing the boundary data before feeding them to the

extrapolation codes. The preprocessing scheme used here (developed by Wiegelmann et al. 2006) seeks to adjust the components of $\mathbf{B}|_{z_0}$, so as to satisfy the first two consistency criteria while minimizing the deviations of $\mathbf{B}|_{z_0}$ from their measured values. During this preprocessing step, spatial smoothing is also applied to $\mathbf{B}|_{z_0}$ to attenuate some of the small-scale magnetic fluctuations that likely die off shortly above the photosphere.

Finally, we apply the various NLFFF algorithms to these boundary and initial data. Several methods for calculating NLFFF models of the coronal magnetic field have been developed and implemented in recent years, including (1) the optimization method, in which the solution field is evolved to minimize a volume integral such that, if it becomes zero, the field is divergence free and force free (Wheatland et al. 2000; Wiegelmann 2004); (2) the evolutionary magnetofrictional method, which solves the magnetic induction equation using a velocity field that advances the solution to a more force-free state (Yang et al. 1986; Valori et al. 2007); and (3) Grad–Rubin-style current-field iteration procedures, in which currents are added to the domain, and the magnetic field is recomputed in an iterative fashion (Grad & Rubin 1958; Amari et al. 2006; Wheatland 2006). Some of these methods have been implemented by multiple authors. For brevity, we omit detailed explanations of these numerical schemes as implemented here and instead direct the reader to Schrijver et al. (2006) and Metcalf et al. (2008), and references therein.

Although these methods work well when applied to simple test cases (Schrijver et al. 2006), we have found that the results from each of the methods typically are not consistent with each other when applied to solar data. The resulting magnetic field configurations differ both qualitatively (e.g., in their connectivity) and quantitatively (e.g., in the amount of magnetic energy contained within them). In discussing the results from the solar-like test case of Metcalf et al. (2008), we described some likely causes of such discrepancies amongst the models. In what follows, we illustrate these problems in greater detail using the (solar) data set at hand.

3. COMPARISON WITH XRT AND STEREO LOOPS

The results of twelve extrapolations for AR 10953 (including the potential field), based on the data preparation steps described in Section 2, are summarized in Table 1 and Figure 2. Table 1 contains domain-averaged metrics characterizing the center of the active region (corresponding to the region surrounding the leading, negative-polarity sunspot), and Figure 2 shows representative field lines in this same volume for each of these models. This central region is a $160 \times 160 \times 160$ pixel volume, chosen to cover the portion of the lower boundary containing much of *Hinode*/SOT–SP magnetogram data (i.e., where we have some knowledge about the currents passing through the photosphere), and is fully contained within the larger $320 \times 320 \times 256$ pixel computational domain.

The models considered in Table 1 and Figure 2 are the current-field iteration method as run by Wheatland using the values of α in either the negative or positive polarity (hereafter “Wh[−]” and “Wh⁺,” respectively); the finite-element Grad–Rubin-style method (FEMQ in Amari et al. 2006) run using two different parameter sets by Amari (“Am1[−]” and “Am2[−]”); the vector-potential Grad–Rubin-like method (XTRAPOL in Amari et al. 2006) by Canou (“Can[−]”), or by Régner using the values of α in either the positive (“Rég⁺”) or negative (“Rég[−]”) polarity; the optimization method using grid refinement as run by Wiegelmann (“Wie”) or McTiernan (“McT”), or no grid

Table 1
NLFFF Model Extrapolation Metrics^a for AR 10953

Model ^b	E/E_{pot}^c	$\langle \text{CW} \sin \theta \rangle^d$	$\langle f_i \rangle^e (\times 10^8)$	$\langle \phi \rangle^f$
Pot	1.00	...	0.02	24°
Wh ⁺	1.03	0.24	7.4	24°
Tha	1.04	0.52	34.0	25°
Wh [−]	1.18	0.16	1.9	27°
Val	1.04	0.26	71.0	28°
Am1 [−]	1.25	0.09	0.72	28°
Am2 [−]	1.22	0.12	1.7	28°
Can [−]	1.24	0.09	1.6	28°
Wie	1.08	0.46	20.0	32°
McT	1.15	0.37	15.0	38°
Rég [−]	1.04 ^g	0.37	6.2	42°
Rég ⁺	0.87 ^g	0.42	6.4	44°

Notes.

^a All metrics were evaluated over a $160 \times 160 \times 160$ pixel comparison volume (whose base overlaps much of the *Hinode*/SOT–SP scan area and is shown as a dotted line in Figures 1(d) and (e)), with the exception of $\langle \phi \rangle$, for which the full $320 \times 320 \times 256$ pixel computational domain was used. The models are listed in order of $\langle \phi \rangle$.

^b As listed in Section 3, the models are the initial potential solution (“Pot”); the current-field iteration method as run by Wheatland using the values of α in the negative (“Wh[−]”) or positive (“Wh⁺”) polarity; the finite-element Grad–Rubin-style method as run by Amari (“Am1[−]” and “Am2[−]”); the vector-potential Grad–Rubin-like method by Canou (“Can[−]”), or by Régner using the values of α in the negative (“Rég[−]”) or positive (“Rég⁺”) polarity; the optimization method using grid refinement as run by Wiegelmann (“Wie”) or McTiernan (“McT”), or no grid refinement as run by Thalmann (“Tha”); and the magnetofrictional method using grid refinement as run by Valori (“Val”).

^c E/E_{pot} is the total magnetic energy relative to the initial potential field solution for the comparison volume.

^d The $\langle \text{CW} \sin \theta \rangle$ metric is the current weighted average of $\sin \theta$, where θ is the angle between \mathbf{B} and \mathbf{J} in each model (with $0^\circ \leq \theta \leq 180^\circ$). For perfectly force-free fields, $\langle \text{CW} \sin \theta \rangle = 0$.

^e The $\langle |f_i| \rangle$ metric is the mean over all pixels i in the comparison volume of the absolute fractional flux ratio $|f_i| = |(\nabla \cdot \mathbf{B})_i| / (6|\mathbf{B}_i|/\Delta x)$, where Δx is the grid spacing. The $\langle |f_i| \rangle$ metric is a measure of how well $\nabla \cdot \mathbf{B} = 0$ is satisfied in the models (see Equation (15) of Wheatland et al. 2000), with divergence-free fields having $\langle |f_i| \rangle = 0$.

^f The quantity $\langle \phi \rangle$ is the mean difference in angle between the stereoscopically determined loops and the NLFFF model field lines (with $0^\circ \leq \phi \leq 90^\circ$), averaged over the full NLFFF computational domain.

^g The Rég[−] and Rég⁺ solutions use closed boundary conditions for the side and top surfaces through which no magnetic flux is transmitted, and thus are associated with a different potential field than the Pot solution. When comparing the Rég[−] and Rég⁺ solutions to the potential field associated with these closed boundary conditions, the values of E/E_{pot} are 1.23 and 1.04, respectively.

refinement as run by Thalmann (“Tha”); the magnetofrictional method using grid refinement as run by Valori (“Val”); and the initial potential solution (“Pot”).

We find that the Am1[−], Am2[−], Can[−], and Wh[−] current-field iteration models contain between 18% and 25% more energy than the potential solution, and have smaller residual Lorentz forces and smaller average $\nabla \cdot \mathbf{B}$ than the other models. In addition, the Am1[−], Am2[−], and Can[−] models find a strongly twisted flux rope in equilibrium, whose foot points are anchored southeast of the main spot (mostly outside of the core volume shown in Figure 2), a feature which was anticipated by the analysis of Okamoto et al. (2008). Models using the optimization method (McT, Wie, and Tha) contain between 4% and 15% more energy than the potential solution, but possess more residual Lorentz forces than the current-field iteration solutions. The magnetofrictional model (Val) has

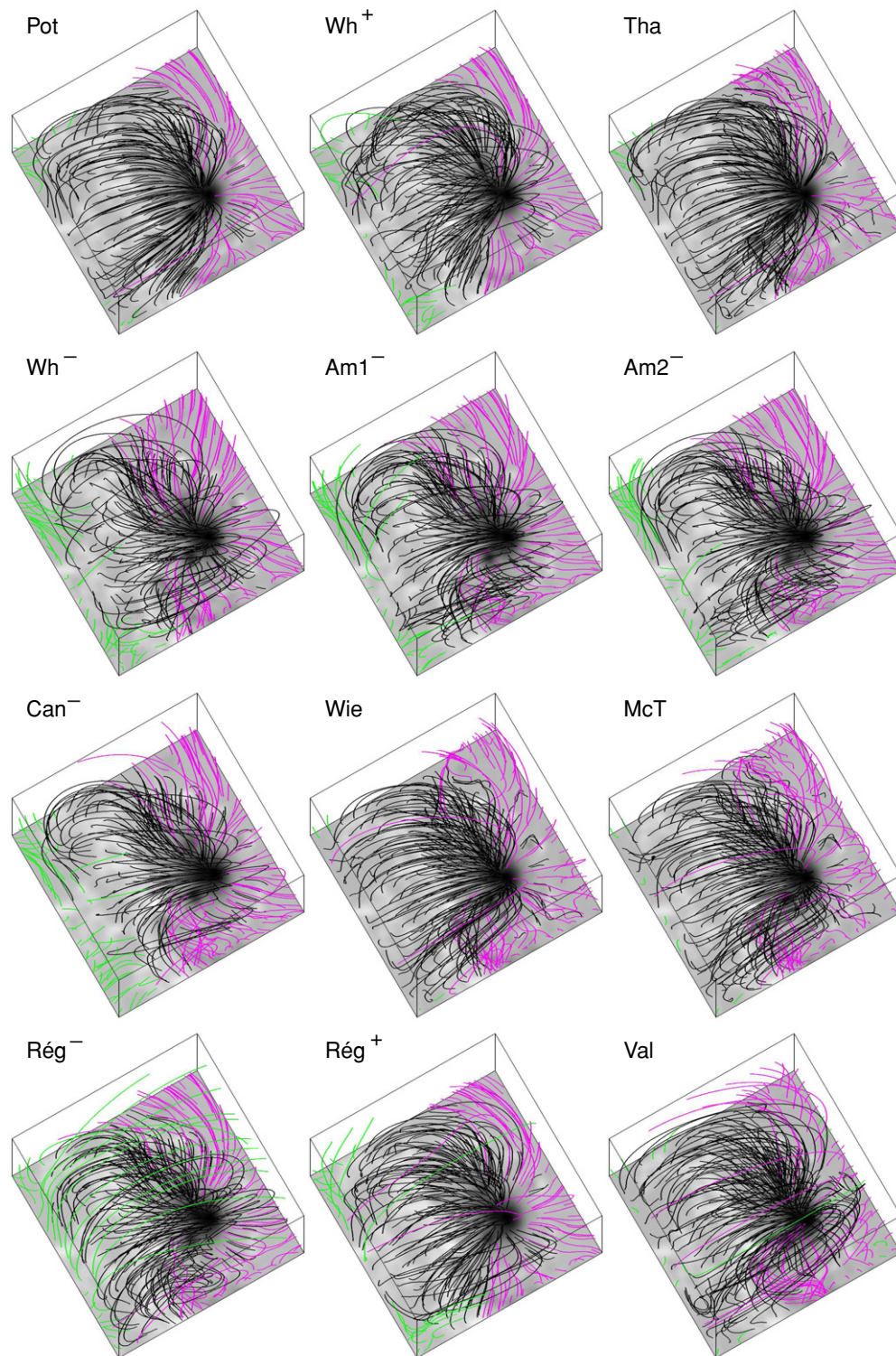


Figure 2. Representative field lines in the central portion of the active region for each NLFFF model listed in Table 1. The cubes shown here comprise the same $160 \times 160 \times 160$ pixel subvolumes excerpted from the full $320 \times 320 \times 256$ pixel computational domain. (The base of this subvolume is the region indicated by dotted lines in Figures 1(d) and (e).) The starting locations for the integration of the field lines are the same in each case, and form an array of regularly spaced grid points located near the lower boundary of the volume. Black field lines indicate (closed) lines that intersect the lower boundary twice, and red and green field lines represent field lines that leave the box through either the sides or top, with color indicative of polarity.

4% more energy than the potential solution, but has larger values of $\nabla \cdot \mathbf{B}$ than the optimization or current-field iteration solutions. Based on the results summarized in Table 1, the excess magnetic energy (above the potential field) for this active region could be anywhere from near zero to about 25%

of the potential field energy. However, it is also possible that the excess energy is significantly larger than 25% when taking into account the uncertainty associated with the inconsistency between the boundary data and the force-free model assumption (see Section 4.3).

Because of these differences in the resulting NLFFF models of AR 10953, we perform a goodness-of-fit test to determine which of the NLFFF models is the best approximation to the observed coronal magnetic field. In the earlier study of Schrijver et al. (2008), we performed this test in both a qualitative and quantitative manner using EUV and X-ray imagery, provided respectively by the *Transition Region and Coronal Explorer (TRACE)* and *Hinode/XRT* instruments, by determining which model possessed field lines that were more closely aligned with the projected coronal loop structures visible in the (two-dimensional) image plane. Models for which most field lines appeared to be aligned with loops were considered good approximations to the actual coronal magnetic field. Locations where the field was noticeably sheared or twisted were of particular interest because such patterns are usually indicative of the presence of currents (which the modeling seeks to ascertain). More weight was typically given to regions connected to places at the photospheric boundary where J_z is found to be high, whereas coronal loops located in the periphery of the active region with footpoints located where J_z was lower were likely to be less sensitive to the presence of currents elsewhere in the active region. All such comparisons with coronal loops rest on the assumption that the plasma responsible for the emission is aligned with the coronal magnetic field and that this field is in a force-free state.

For AR 10953, we overlaid field lines from all of the NLFFF models (as well as the potential field model) on top of the time-averaged *Hinode/XRT* image shown in Figure 1(a), and used the same criteria listed above to qualitatively determine the better-matching models. We subjectively judged the field lines in the Wh^- , $Am1^-$, $Am2^-$, and Can^- models to be more closely aligned with the XRT loops than any of the others. An overlay of field lines from the Wh^- model is shown in Figure 1(b). This judgment is based on good alignment with the tightly curved X-ray loops north of the sunspot (which is visible in the coaligned magnetogram of this region shown in Figure 1(d)), together with a reasonably good match of the loop arcade and fan structures to the south and west of the sunspot. This judgment is also based on side-by-side comparisons of field line overlays amongst the various candidate models (including the potential field model), from which a relative ranking was determined. The models listed above came out on top in both instances.

With the aim of determining more quantitatively the best-fit model(s) for AR 10953, we also compared the model field lines to three-dimensional trajectories of loop paths. We are able to do this because AR 10953 was observed by the twin *Solar Terrestrial Relations Observatory (STEREO)* spacecraft, one of which leads the Earth in its orbit around the Sun, and the other of which trails the Earth. As part of the Sun Earth Connection Coronal and Heliospheric Investigation (SECCHI) instrument suite (Howard et al. 2008), each *STEREO* spacecraft contains an Extreme Ultraviolet Imager (EUVI). The angular separation of the two *STEREO* spacecraft at the time AR 10953 was on disk (of about 7°) was favorable for stereoscopically determining the three-dimensional trajectories of loops observed in the 171 Å, 195 Å, and 284 Å channels of EUVI. The coordinates of these loop trajectories were obtained by triangulating the positions of common features visible in pairs of concurrent EUVI images using the method described by Aschwanden et al. (2008).

Unfortunately, most of the loops visible in the three EUVI wavebands lie outside of the central region of AR 10953 (Figure 1(c)), and thus do not overlap the region for which the vector magnetogram data are available (Figures 1(d) and (e)).

The main reason is that loops located closer to the centers of the active regions tend to emit more in X-ray passbands than in EUV passbands. In addition, large loops at the periphery of active regions are generally easier to reconstruct with stereoscopy, while small loops in the centers of active regions are more difficult to discern from underlying bright features (such as moss) and thus cannot unambiguously be triangulated. However, the outlying loops evident in AR 10953 should still sense the presence of currents in the center of the active region, due to Ampère's law, and thus might be useful for quantitatively determining the best-matching NLFFF model for this active region. We infer that currents must be present in the AR 10953 corona for two reasons. First, most of the strong vertical currents in the J_z map are located in the central portion of the active region (as illustrated in Figure 3) and presumably flow upward into the corona. Second, field lines from the potential model do not qualitatively match the X-ray and EUV loops as well as field lines from the Wh^- , $Am1^-$, $Am2^-$, and Can^- models, which are our most nonpotential models and evidently contain currents strong enough to affect the trajectories of many field lines in the central portion of this active region (see Figure 2).

To quantitatively compare the *STEREO* loops and the NLFFF model field lines, we determine the (positive) angle ϕ between the *STEREO*-loop and the model field line trajectories subtended at all *STEREO*-loop points lying inside the full $320 \times 320 \times 256$ pixel NLFFF computational domain. We then computed the mean of these angles, yielding for each model the domain-averaged misalignment angle metric $\langle \phi \rangle$ listed in Table 1. We find that, at least by this particular quantitative measure, none of the NLFFF models improve upon the value of $\langle \phi \rangle = 24^\circ$ found for the potential field model, although several models (including the qualitatively better-fitting models discussed earlier) are comparable. We discuss reasons why none of the models improved upon the potential field metric for $\langle \phi \rangle$ in Section 4.2.

4. DISCUSSION

Given the boundary conditions produced using the data preparation process described in Section 2, the various NLFFF algorithms converged to different solutions for the coronal field above AR 10953. A few of the models appear to match the loop structures in the *Hinode/XRT* image, but none of them were able to improve upon the potential field in their alignment with the three-dimensional loop trajectories inferred from *STEREO/SECCHI-EUVI*. In attempting to find a consensus model, we also applied the NLFFF algorithms to different boundary data generated using variants of the data preparation process. These variations, described in Section 4.1, were run in parallel to those analyzed in Section 3, but they too did not produce a viable model.

This inability to generate models that both qualitatively and quantitatively match the coronal loops paths is disappointing, especially given the generally successful application of these algorithms to test cases with known solutions (Schrijver et al. 2006), including a solar-like test case with quasi-realistic forcing in the lower layers that was meant to approximate some of the forces acting in the solar chromosphere (Metcalf et al. 2008). While we realistically expect the various methods to yield somewhat different solutions, we cannot fully ascribe the broad range of inconsistencies in the solutions solely to algorithmic differences. This causes us to examine the entire NLFFF modeling process from beginning to end, and in so

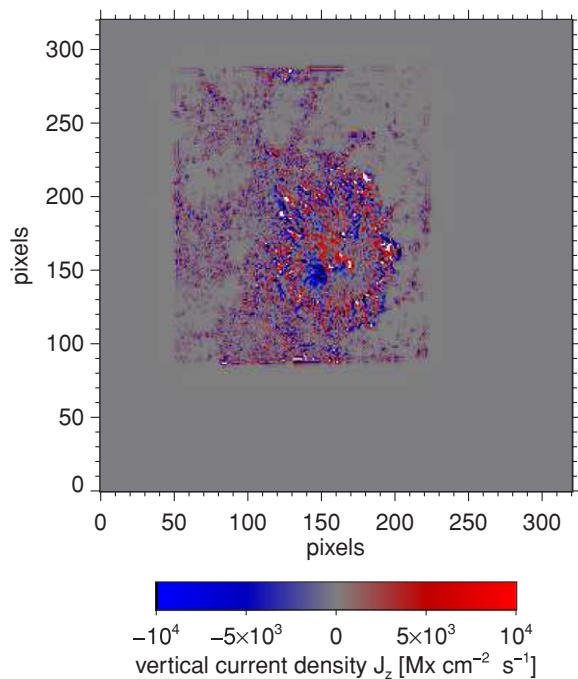


Figure 3. Map of the vertical component of the electric current density J_z at the lower bounding surface as determined from *Hinode*/SOT-SP vector-field measurements (i.e., prior to preprocessing). The values of B_x and B_y , and therefore J_z , outside of the region containing vector magnetogram data are unknown and have been zeroed out. Saturation of the color table is indicated by black or white hues. The pixel scale is 580 km per pixel.

doing we have identified several additional factors that likely also impact our ability to produce robust models. These factors are discussed further in Sections 4.2 and 4.3.

4.1. Data Preparation Variations

We applied the NLFFF algorithms to boundary data produced using eleven variations of the data preparation process, of which only one was outlined in Section 2. Variations involved substituting a different procedure to remove the 180° ambiguity of the measured transverse vector field, and/or using different versions of the standard preprocessing algorithm. In total, about 60 different NLFFF models for AR 10953 were calculated. (Not all algorithms were run on all of the available boundary data sets.)

The first variant entailed using a different algorithm to remove the 180° ambiguity inherent in the vector magnetogram inversion process. Although there are, in fact, several algorithms to do this, we chose as an alternative to AZAM to employ the automated University of Hawaii Iterative Method (UHIM) (Canfield et al. 1993) because it has been used extensively in the literature and also scored highly amongst other ambiguity resolution algorithms (Metcalfe et al. 2006). We found that, while differences exist in, for example, field line trajectories near regions where the ambiguity was resolved differently, the volume-integrated metrics discussed in Section 3 and shown in Table 1 were largely similar for both the AZAM- and UHIM-disambiguated boundary data.

The second variant involved a new version of the method used to preprocess the values of $\mathbf{B}|_{z_0}$ to make the boundary data more consistent with a force-free solution. Our standard scheme pivots and smooths the components of $\mathbf{B}|_{z_0}$ so that the integrated magnetic forces and torques in the overlying volume are reduced as much as possible, while also retaining some fidelity to the measured vector field. For AR 10953, we

also experimented with a preprocessing scheme (described by Wiegelmann et al. 2008) that, in addition to the above, seeks to align the horizontal components of $\mathbf{B}|_{z_0}$ with fibrils seen in contemporaneous images of $H\alpha$. The motivation for this additional preprocessing constraint is to produce boundary data as close as possible to the force-free field expected to exist at the chromospheric level (to which the $H\alpha$ fibrils are assumed parallel). We found, however, that using $H\alpha$ -fibril information (observed by the Narrowband Filter Imager of *Hinode*/SOT) did not make a significant difference in the domain-averaged metrics used to characterize the various extrapolation models, although we intend to experiment further with this preprocessing scheme as it is somewhat new.

The third variant was to use the method of preprocessing described by Fuhrmann et al. (2007), the goals of which are the same as the Wiegelmann et al. (2006), but which uses a simulated annealing numerical scheme to find the optimal $\mathbf{B}|_{z_0}$ field. As with the other variations, using this alternate preprocessing scheme did not much affect the resulting global metrics (M. Fuhrmann et al. 2009, in preparation).

4.2. Field-of-View Issues

The *Hinode*/SOT-SP vector magnetogram data span only the central portion of the AR 10953, and thus do not cover all of the weaker field and plage that surround the active region center. Here, as in the Schrijver et al. (2008) case, we chose to extend the NLFFF computational domain and embed the vector data in a larger line-of-sight magnetogram. One benefit of such embedding is that it places the side and top bounding surfaces farther away from the center of the active region, in locations where the coronal magnetic field is presumed more potential and thus more consistent with the boundary conditions applied there. Another reason is that in earlier test cases using boundary data with known solutions (described by Schrijver et al. 2006), we found that enlarging the NLFFF computational domain improved the solution field in the central region of interest. We attributed this behavior primarily to the sensitivity of the final solution to the specified boundary conditions, and concluded that moving the side and top boundaries farther away from the region of interest improved the resulting models.

However, there is an important difference between these earlier tests and the current case of AR 10953. In the Schrijver et al. (2006) study, vector data for the entire (enlarged) lower boundary were available, and thus the locations of currents penetrating the entire lower bounding surface, over both polarities, were known. In contrast, for AR 10953 we have no information about currents located exterior to the region containing the *Hinode* vector magnetogram data, as shown in Figure 3, and consequently (as stated earlier) the horizontal components of $\mathbf{B}|_{z_0}$ were set to zero in the region outside of the area containing *Hinode*/SOT-SP vector data. This is obviously not correct, but lacking any knowledge of actual horizontal fields there, this approach was presumed to be the least damaging. However, the lack of satisfactory results suggests that the decision to embed may not be as harmless as originally believed.

The ability of the various NLFFF algorithms to find a valid solution ultimately depends upon how they deal with the currents passing through the bounding surfaces of the computational domain. Figure 4 shows maps of the current density integrated vertically through the models. It is evident from these images that algorithms based on similar methods result in models that look similar to each other, but also that there are stark

differences between the locations of the strong currents amongst the different classes of methods.

It is interesting to note that for AR 10953, as for the Schrijver et al. (2008) case, the solutions bearing the best resemblance to the *Hinode*/XRT loops, and here were among the best at matching the *STEREO*-loop trajectories, were calculated using the current-field iteration method. This method differs from the others in that it uses values of J_z and α only in one of the polarities (the well observed leading polarity, in the case of the best-fit models) from the lower boundary, while ignoring such measurements in the opposite polarity. In contrast, the optimization and magnetofrictional methods require that information about currents be available across both polarities.

We suspect that the Wheatland current-field iteration algorithm benefits from the additional space in the solution domain because fewer current-carrying field lines intersect the side boundaries (which causes their values of α to be set to zero). However, the Wiegelmann optimization algorithm, and the Valori magnetofrictional algorithm in particular, perform better when applied to smaller volumes or when the weighting given to the peripheral boundary information is less than that applied to the *Hinode* vector magnetogram data. The bottom row of images in Figure 4 shows that the Valori magnetofrictional algorithm has markedly different behavior depending on the weighting of the peripheral boundary data. The differences are most striking in the area exterior to where the vector magnetogram data are located. Restricting the computational domain to contain only the region overlying the *Hinode*/SOT-SP field of view produces a solution with more intense currents and having fewer Lorentz forces ($\langle CW \sin \theta \rangle = 0.19$) and greater energy ($E/E_{\text{pot}} = 1.12$) than the Val solution. Many of these problems caused by the embedding process are alleviated when vector magnetogram data are provided over a field of view that covers the locations of all relevant currents associated with the region of interest. For active region studies, this often means capturing much of the trailing polarity, which is often more diffuse and extended than the leading polarity.

We therefore conclude that vector magnetogram data of active regions for use by NLFFF modeling efforts need to span much of the area above which currents flow. Coverage of the more diffuse, trailing-polarity fields is likely to be especially important because of the tendency for the trailing-polarity field to contain the endpoints of many field lines that carry significant currents (due to the existence of such currents in the leading polarity, coupled with the assumption that many field lines connect the leading and trailing polarities within the active region of interest).

On a related topic, we suspect that the *STEREO*-loop comparison process described in Section 3 is affected both by the proximity of the *STEREO* loops to the sidewalls of the NLFFF computational domain (where potential field boundary conditions were applied) and by their lying outside of the region for which we have vector magnetogram data (Figures 1(d) and (e)). Consequently, one might not be surprised that the potential model bested the others in matching the *STEREO* loops, but the sizable misalignment angle $\langle \phi \rangle$ of 24° for the potential model seems to suggest that even these outlying *STEREO* loops do carry some currents.

In light of these issues, rather than using the *STEREO*-loop comparison as a discriminator between the collection of NLFFF models, we instead view the collectively poor misalignment angles by the NLFFF models as another indication that the region over which vector magnetogram data are available needs

to be enlarged. Although it is possible to enlarge the NLFFF computational domain (beyond what we have already done) in order to include even more loops observed by *STEREO*, we again emphasize that the added benefit of doing so without additional vector magnetogram data would be minimal because of the lack of further information about currents flowing through the lower boundary. Indeed, we applied the same current-field iteration method used for Wh^- to larger (512×512 pixel) boundary data produced using the same process described in Section 2, and found that the value of $\langle \phi \rangle$ for the identical volume used to compute the values of $\langle \phi \rangle$ in Table 1 remained unchanged.

Lastly, we recognize that, when compared with stronger-field regions, the transverse field components B_t are not measurable with the same degree of certainty in weaker-field regions such as those likely to lie within the enlarged fields of view for which we are advocating. The findings presented here, however, suggest that the NLFFF modeling algorithms would benefit by having these vector magnetic field data available, even if such data possess higher measurement uncertainties than the stronger fields found closer to the centers of most active regions.

4.3. Boundary Data Inconsistencies

In Section 2, we described several conditions that the boundary data $\mathbf{B}|_S$ must satisfy in order to be consistent with a force-free magnetic field. However, these conditions are never guaranteed to be satisfied on the full bounding surface S , which here consists of the vector and line-of-sight magnetogram data for the lower boundary combined with the potential field boundary conditions used for the remainder of the enclosing surface. To partially rectify this problem, we apply preprocessing to these data to thereby adjust the various components of $\mathbf{B}|_{z_0}$ on S such that the boundary data are made more compatible with the equations the NLFFF algorithms seek to solve.

Even after preprocessing, however, the boundary data can be shown to be incompatible with a force-free field. The Wh^- model, which is one of several models judged to match best on a qualitative basis, only uses the α values located in the negative polarity of the active region. However, the algorithm converged to a solution for which the corresponding α values in the positive polarity do not match those indicated by the *Hinode*/SOT-SP data. Figure 5(a) illustrates this problem. There, the α values in the Wh^- model from field lines that intersect the lower boundary in the positive polarity are plotted against the α values at the same boundary points deduced from the preprocessed *Hinode* data. For consistent boundary data, these would be equal. The scatter evident in the figure indicates that the *Hinode* boundary data, even after preprocessing, are inconsistent with a force-free field. Additionally, the difference in the location of currents in the Wh^- and Wh^+ models (and similarly in the Rég^- and Rég^+ models), as evident in Figure 4, may also indicate that the boundary data are inconsistent with a force-free solution.

Figure 5(b) illustrates this effect in a different way. This incompatibility can be illustrated by computing

$$\Phi(\alpha) = \int_S H(\alpha' - \alpha) B_z dx dy, \quad (1)$$

where H is the Heaviside step function, and $B_z(x, y)$ and $\alpha'(x, y)$ are, respectively, the flux density and value of J_z/B_z at each point on the preprocessed *Hinode* boundary map. The function $\Phi(\alpha)$ signifies the net flux in that subarea of the boundary map for which α' is larger than a certain threshold α . When the α -correspondence relation holds, the function $\Phi(\alpha)$ thus possesses

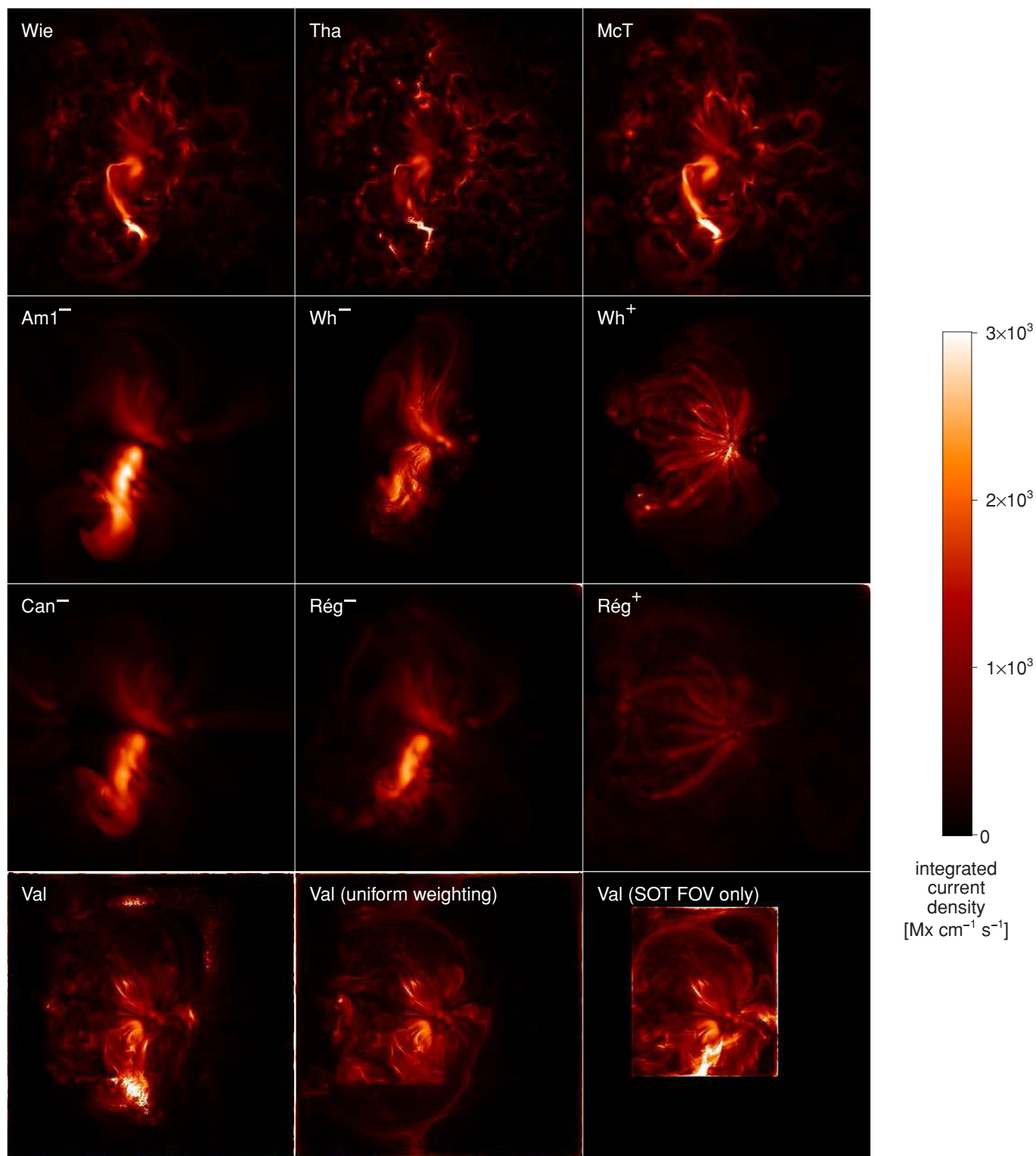


Figure 4. Images showing the magnitude of the current density $|J|$ after integrating vertically through the computational domain for most of the models presented in Figure 2. Algorithms using the same class of method tend to produce similar patterns, as evident in the top row (showing models produced using optimization algorithms) and in the middle two rows (showing models produced using Grad–Rubin-style current-field iteration algorithms). The bottom row illustrates three different versions of the Valori magnetofrictional model, illustrating some of the effects associated with the process of embedding vector magnetogram data into line-of-sight magnetogram data to produce lower-boundary data. Shown are the Val model of Figure 2 which weights more heavily the boundary data inside the *Hinode*/SOT–SP field of view, a model for which the lower-boundary data were weighted uniformly, and a smaller-domain model encapsulating only the volume overlying the *Hinode*/SOT–SP field of view. The integrated current map from the Am2[−] model in Figure 2 is almost identical to that of the Am1[−] model, and is not shown.

a derivative of zero because such correspondence requires, for any interval $d\alpha$, an equal amount of positive and negative flux

passing through that subarea of the boundary map having values of α' between α and $\alpha + d\alpha$. However, Figure 5(b) shows that

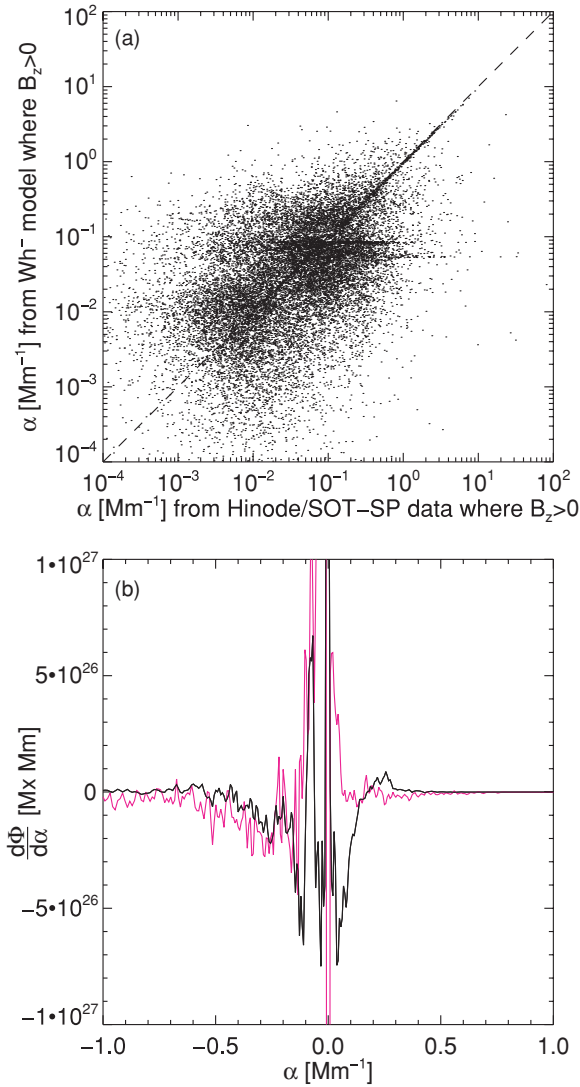


Figure 5. (a) Scatter diagram illustrating the mismatch between the values of α implied by the preprocessed *Hinode*/SOT-SP boundary data $\mathbf{B}|_{z_0}$ for all points having $B_z > 0$, and the values of α for field lines in the Wh^- model intersecting these same points. For a consistent boundary condition where the α -correspondence relation is satisfied, the values of α on each field line in the Wh^- solution (which are taken from the negative-polarity end of the field line) would match the measured value of α found at the positive-polarity end. (b) The differential change $d\Phi/d\alpha$ in net flux Φ integrated over all points having α values greater than the abscissa. The unpreprocessed (red) and preprocessed (black) boundary data for AR 10953 are both shown. Data for which the α -correspondence relation holds have $d\Phi/d\alpha = 0$.

$d\Phi/d\alpha$ is nonzero over most α values for the preprocessed data used here, especially within the range $-0.2 < \alpha < 0.2$ which corresponds to the α values possessed by about 80% of the area of the boundary map. For comparison, the figure includes the function $d\Phi/d\alpha$ for the unpreprocessed data set.

The various methods deal with the lack of α correspondence in the boundary data in different ways. Current-field iteration methods allow the α -correspondence condition to be met by ignoring the values of α in one polarity. However, only limited uniqueness results have been found for this approach, and even existence results are limited to the case of an unbounded domain (see Amari et al. 2006). It is well known that the current-field iteration method fails to converge in some cases, and this may be due to the absence of a solution, or the absence of a unique

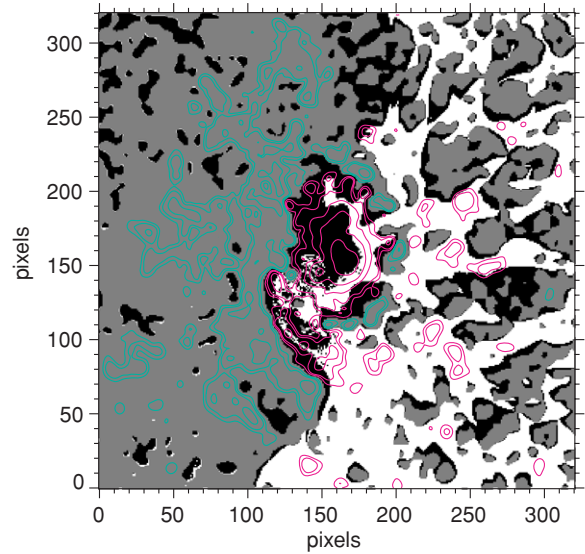


Figure 6. Sensorship map for the Wh^- model. Pixels are gray in the positive polarity of B_z and are either black or white in the negative polarity. White pixels indicate the locations of field lines for which α was censored (set to zero); black pixels indicate locations where $\alpha \neq 0$. Contours of B_z are overlaid, with green and red contours located in positive and negative polarity regions, respectively. Contour levels are at $\pm\{100, 200, 500, 1000, 2000\} \text{ Mx cm}^{-2}$. The pixel scale is 580 km per pixel.

solution. In Wheatland's implementation of this method, if the solution does not converge, values of α are censored (set to zero) in the polarity defining the currents going into the corona. The censorship is imposed at boundary points with $|B_z|$ less than a threshold value, and that value is increased as required. Additional censorship is also imposed such that field lines intersecting the side and top boundaries carry no current. In practice, it is found that such reduction of the currents flowing into the domain can lead to convergence. The Wh^- model, for example, censored almost half of the values of α in the negative polarity (corresponding to 43% of the negative-polarity flux) before convergence was achieved, as illustrated in Figure 6. Valori's magnetofrictional method is prevented from relaxing past an equilibrium state in which the continual injection of inconsistencies into the model (at the boundaries) is balanced by their removal via diffusion. Wiegelmann's optimization method does not reach as well relaxed of a force-free state as some of the other models, even though it disregards some of the boundary mismatches via the tapered nature of the weighting functions toward the edges of the model volume.

There are several reasons why the boundary conditions used for this study (and other active region studies) might not satisfy the force-free consistency relations. The most conspicuous reason is that the photospheric layers of the Sun, from which originate the *Hinode*/SOT-SP magnetogram data used here, do contain Lorentz, buoyancy, and pressure gradient forces and thus are not force free to begin with (Metcalf et al. 1995; Gary 2001). Additionally, measurement uncertainties in the components of $\mathbf{B}|_{z_0}$ preclude accurate determinations of J_z (and thus α) on the lower boundary because of the need to take derivatives of the horizontal components of $\mathbf{B}|_{z_0}$. Another reason is that measurements of the current density normal to the enclosing surface are unavailable over much of S due to the lack of vector magnetogram data above the photosphere. Another reason is that the modeling implicitly assumes that the boundary data span a planar surface, and do not take into account effects present in vector magnetograms such as the Wilson depression in sunspots

and the broad range of line formation heights across the line. Yet another reason is that the inversion techniques that produce the vector magnetogram measurements do not fully take into account the multiple components of thin, narrow strands of interleaved magnetic fields that characterize sunspot penumbrae (Title et al. 1993; Bellot Rubio et al. 2004; Shimizu et al. 2008). We thus conclude that the NLFFF modeling process needs to account for these intrinsic uncertainties in the boundary data, which include everything from measurement uncertainties to the lack of knowledge about how to infer the magnetic field in the force-free region at the base of the corona from the observed photospheric field maps.

5. CONCLUSIONS

We have attempted to model the coronal magnetic field overlying AR 10953 by applying a suite of NLFFF algorithms to the photospheric vector field measured using *Hinode*/SOT-SP. These data were remapped, embedded, and preprocessed in various ways in order to produce boundary data for this active region that were also consistent with the force-free assumption. From these boundary data, about 60 different NLFFF models were constructed.

The resulting variations in these models prompted us to validate the results against images of coronal loops evident in EUV or X-ray images. The goodness of fit was first determined in a qualitative manner by overlaying NLFFF-model field lines on *Hinode*/XRT imagery. This comparison indicated that some models contain field lines that are aligned with the observed loop structures. However, conclusive determinations of best-matching models, based solely on such overlays, remained difficult because of the indistinct nature of many coronal loops, especially those located near the center of AR 10953 where many of the currents are presumed to lie.

We then turned to stereoscopic determinations of three-dimensional loop paths as a way to quantitatively assess the goodness of fit. This comparison was also inconclusive, because the loops traced stereoscopically in the *STEREO*/SECCHI-EUVI observations were restricted to the outermost domain of the active region. This meant that those loops that did fall in the NLFFF computational domain lay close to the edge of the computational volume, where model field lines either leave the domain or run close to the side boundaries. We suspect this quantitative comparison was at least partially compromised by these effects, due to the model fields being sensitive to the way in which the side boundary information is incorporated and to their being located above the portion of the lower boundary for which *Hinode*/SOT-SP vector magnetogram data were not available.

As exemplified by the qualitative and quantitative comparisons presented here, we find that it remains difficult to construct and validate coronal magnetic field models of solar active regions that can reliably be used for detailed analyses of a quantitative nature. Our experience with modeling test cases with known solutions had shown that the various algorithms do work when given consistent boundary conditions. This led us to examine thoroughly the entire NLFFF modeling framework in order to identify problematic issues that impact our ability to build useful models of the solar coronal field. The results of this examination leave us with several possibilities. First, it may be that useful NLFFF extrapolations based on currently available signal-to-noise levels, preprocessing procedures, fields of view, and observable fields are intrinsically infeasible. A second (and more hopeful) possibility is that NLFFF extrapolations need

both much larger fields of view to better constrain the long field lines high over a region or to distant neighboring regions, and enough spatial resolution to resolve the spatial distribution of current densities on the boundaries. Third, NLFFF algorithms need to accommodate the fact that the boundary conditions contain (sometimes significant) uncertainties, either from the measurement process (e.g., signal-to-noise issues or inadequate resolution of the 180° ambiguity), or from physical origins (e.g., variations in the line formation height, or most prominently the non-force-free nature of photospheric vector magnetograms).

The second possibility can be tested empirically. One way to do this with current codes and instrumentation is to obtain vector magnetic observations of a substantially smaller active region and its wide surroundings. This will place the side boundaries relatively farther away from the region of interest, while remaining compatible with the range and resolution of, e.g., the *Hinode*/SOT-SP and with the Cartesian nature of the available modeling codes.

To address the third possibility, we have several avenues available. Simple ways to account for boundary data uncertainties include introducing a position-dependent weighting function used in relaxation methods, or modifying the selection criteria for the α field in the current-field iterative method. Additionally, the preprocessing of the raw vector data needs to better approximate the physics of the photosphere-to-chromosphere interface in order to transform the observed photospheric field to a realistic approximation of the overlying near-force-free field at the base of the corona. One way to do that without resorting to more computationally intensive MHD models is to use the magneto-hydrostatic concept (e.g., Wiegmann & Neukirch 2006) and approximate the stratifications for the flux tubes and their surroundings (or the strongly and weakly magnetic regions) separately.

Finally, in light of our findings in this study and in consideration of the aforementioned goal of constructing models that provide useful estimates of physical quantities of interest, we thus recommend that a particular force-free extrapolation should not be considered a consistent model of an active region corona unless the following indicators (at a minimum) are satisfied: (1) good alignment of modeled field lines to the coronal loops observed on the solar disk; (2) acceptable agreement of the α -correspondence relation by having similar values of α at both ends of all closed field lines, and acceptable agreement with the boundary values of α from the data; while (3) still realizing low values of the NLFFF metrics $\langle CW \sin \theta \rangle$ and $\langle |f_i| \rangle$.

We gratefully acknowledge Professor Sami Solanki and the Max-Planck-Institut für Sonnensystemforschung in Katlenburg-Lindau, Germany, for their hospitality during our most recent workshop, at which the ideas presented in this article were discussed and refined. *Hinode* is a Japanese mission developed and launched by ISAS/JAXA (Japan), with NAOJ as domestic partner and NASA (USA) and STFC (UK) as international partners. It is operated by these agencies in cooperation with ESA and NSC (Norway). The *STEREO*/SECCHI data used here are produced by an international consortium of the Naval Research Laboratory (USA), Lockheed Martin Solar and Astrophysics Laboratory (USA), NASA/Goddard Space Flight Center (USA), Rutherford Appleton Laboratory (UK), University of Birmingham (UK), Max-Planck-Institut für Sonnensystemforschung (Germany), Centre Spatial de Liège (Belgium), Institut d'Optique Théorique et Appliquée (France), and Institut d'Astrophysique Spatiale (France). M.L.D., C.J.S., G.B., and

K.D.L. were supported by Lockheed Martin Independent Research Funds. M.L.D. was also supported by NASA contract NNM07AA01C to Lockheed Martin. J.M.M. was supported by NASA grants NNG05144G and NNX08A156G. S.R. acknowledges the financial support of the UK STFC. J.K.T. acknowledges support from DFG grant WI 3211/1-1. G.V. was supported by DFG grant HO 1424/9-1. T. W. acknowledges support from DLR grant 50 OC 0501. P.A.C. is an IRCSET Government of Ireland Scholar. T.T. acknowledges support from the International Max Planck Research School on Physical Processes in the Solar System and Beyond.

Facilities: Hinode, SOHO, STEREO

REFERENCES

- Aly, J. J. 1984, *ApJ*, **283**, 349
 Aly, J. J. 1989, *Sol. Phys.*, **120**, 19
 Amari, T., Boulmezaoud, T. Z., & Aly, J. J. 2006, *A&A*, **446**, 691
 Aschwanden, M. J., Wülser, J.-P., Nitta, N. V., & Lemen, J. R. 2008, *ApJ*, **679**, 827
 Bellot Rubio, L. R., Balthasar, H., & Collados, M. 2004, *A&A*, **427**, 319
 Borrero, J. M., Tomeczyk, S., Norton, A., Darnell, T., Schou, J., Scherrer, P., Bush, R., & Liu, Y. 2007, *Sol. Phys.*, **240**, 177
 Canfield, R. C. 1993, *ApJ*, **411**, 362
 Fuhrmann, M., Seehafer, N., & Valori, G. 2007, *A&A*, **476**, 349
 Gary, G. A. 2001, *Sol. Phys.*, **203**, 71
 Golub, L., et al. 2007, *Sol. Phys.*, **243**, 63
 Grad, H., & Rubin, H. 1958, in *Peaceful Uses of Atomic Energy: Proc. Second UN International Atomic Energy Conference*, 31 (Geneva: UN), 190
 Howard, R. A., et al. 2008, *Space Sci. Rev.*, **136**, 67
 Klimchuk, J. A., Canfield, R. C., & Rhoads, J. E. 1992, *ApJ*, **385**, 327
 McClymont, A. N., Jiao, L., & Mikić, 1997, *Sol. Phys.*, **174**, 191
 Metcalf, T. R., et al. 2008, *Sol. Phys.*, **247**, 269
 Metcalf, T. R., Jiao, L., McClymont, A. N., Canfield, R. C., & Uitenbroek, H. 1995, *ApJ*, **439**, 474
 Metcalf, T. R., et al. 2006, *Sol. Phys.*, **237**, 267
 Molodenskii, M. M. 1969, *SvA*, **12**, 585
 Okamoto, T. J., et al. 2008, *ApJ*, **673**, L215
 Régnier, S., & Amari, T. 2004, *A&A*, **425**, 345
 Régnier, S., Amari, T., & Kersalé, E. 2002, *A&A*, **392**, 1119
 Régnier, S., & Canfield, R. C. 2006, *A&A*, **451**, 319
 Sakurai, T. 1981, *Sol. Phys.*, **69**, 343
 Scherrer, P. H., et al. 1995, *Sol. Phys.*, **162**, 129
 Schrijver, C. J., et al. 2008, *ApJ*, **675**, 1637
 Schrijver, C. J., et al. 2006, *Sol. Phys.*, **235**, 161
 Shimizu, T., et al. 2008, *ApJ*, **680**, 1467
 Skumanich, A., & Lites, B. W. 1987, *ApJ*, **322**, 473
 Title, A. M., Frank, Z. A., Shine, R. A., Tarbell, T. D., Topka, K. P., Scharmer, G., & Schmidt, W. 1993, *ApJ*, **403**, 780
 Tsuneta, S., et al. 2008, *Sol. Phys.*, **249**, 167
 Valori, G., Kliem, B., & Fuhrmann, M. 2007, *Sol. Phys.*, **245**, 263
 Wheatland, M. S. 2006, *Sol. Phys.*, **238**, 29
 Wheatland, M. S., Sturrock, P. A., & Roumeliotis, G. 2000, *ApJ*, **540**, 1150
 Wiegelmann, T. 2004, *Sol. Phys.*, **219**, 87
 Wiegelmann, T., Inhester, B., & Sakurai, T. 2006, *Sol. Phys.*, **233**, 215
 Wiegelmann, T., Lagg, A., Solanki, S. K., Inhester, B., & Woch, J. 2005, *A&A*, **433**, 701
 Wiegelmann, T., & Neukirch, T. 2006, *A&A*, **457**, 1053
 Wiegelmann, T., Thalmann, J. K., Schrijver, C. J., DeRosa, M. L., & Metcalf, T. R. 2008, *Sol. Phys.*, **247**, 249
 Yang, W. H., Sturrock, P. A., & Antiochos, S. K. 1986, *ApJ*, **309**, 383